

## Article

# Comparison of Several Energy-Efficient Control Laws Using Energetic Macroscopic Representation for Electric Vehicles

Jean-Mathieu Bourgeot , Romain Leclerre and Emmanuel Delaleau \* 

ENI Brest, UMR CNRS 6027, IRDL, F-29 200 Brest, France; bourgeot@enib.fr (J.-M.B.)

\* Correspondence: delaleau@enib.fr

**Abstract:** Energy transition and decarbonization present significant challenges to transportation. Electric machines, such as motors and generators, are increasingly replacing internal combustion engines to reduce greenhouse gas emissions. This study focuses on enhancing the energy efficiency of electric machines used in vehicles, which are predominantly powered by batteries with limited energy capacity. By investigating various control strategies, the aim is to minimize energy losses and improve overall vehicle performance. This research examines two types of electric motors: Permanent Magnet Synchronous Motor (PMSM) and Induction Motor (IM). Real-time loss measurements were conducted during simulated driving cycles, including acceleration, constant speed, and braking phases, to mimic typical driving behavior. The simulation utilized characteristics from commercial vehicles, specifically the Renault Zoé and Bombardier eCommander, to assess the controls under different configurations. This study employed the Energetic Macroscopic Representation (EMR) formalism to standardize the analysis across different motors and controls. The results demonstrate significant loss reductions. The controls investigated in this study effectively reduce energy losses in electric motors, supporting their applicability in the automotive industry.

**Keywords:** Energetic Macroscopic Representation; electrical motor control; flux management; reduction in losses



**Citation:** Bourgeot, J.-M.; Leclerre, R.; Delaleau, E. Comparison of Several Energy-Efficient Control Laws Using Energetic Macroscopic Representation for Electric Vehicles. *Energies* **2024**, *17*, 4945. <https://doi.org/10.3390/en17194945>

Academic Editor: Chunhua Liu

Received: 30 August 2024

Revised: 25 September 2024

Accepted: 28 September 2024

Published: 2 October 2024



**Copyright:** © 2024 by the authors. Licensee MDPI, Basel, Switzerland. This article is an open access article distributed under the terms and conditions of the Creative Commons Attribution (CC BY) license (<https://creativecommons.org/licenses/by/4.0/>).

## 1. Introduction

Energy transition and carbonation are significant challenges to the future of transportation. The use of electric machines—motors and generators—is increasing in order to replace more polluting internal combustion engines, which emit greenhouse gases.

When these machines are used in the transportation sector, they are mostly powered by a battery with limited energy capacity. The technologies used in these batteries vary, including Nickel-Cadmium (Ni-Cd), Lithium-Ion (Li-Ion), or, more recently, Sodium-Ion (Na-Ion) batteries. Their purpose is to convert chemical energy into electrical energy. Two important parameters to consider are the maximum power the battery can provide and its capacity. These elements are crucial for the vehicle as they define its performance.

However, the role of the battery is almost exclusively reserved for powering the motor, with onboard equipment consuming very little current. Consequently, it is deduced that the motor must consume as little energy as possible to increase the power supply of the battery duration and, consequently, the distance traveled. Similarly, energy savings translate into financial savings on recharging. It should be noted that the project will focus solely on the “tank to wheel” aspect.

In this context, this study aims to report on energy-efficient controls for electric machines in order to reduce losses across all operating conditions. The topic is deliberately open to exploring a wide range of different controls and covering a significant portion of what can be conducted in electric propulsion.

Their various applications range from electric scooters to electric cars, as well as electric ships (not addressed in this article). Reducing the losses of each of these means of transportation helps decrease the energy consumption from an ecological perspective.

As mentioned previously, the objective of this work is to reduce the energy losses of electric motor vehicles. Recent articles in this ecological perspective focus only on a single control and a single motor, whereas here, the aim is to compare these works. Two motors will be the objects of this study. These motors were chosen because they are essential and still widely used today: the Permanent Magnet Synchronous Motor (PMSM) and the Asynchronous Motor, also called the Induction Motor.

The losses of the different motors will be measured in real time during cycles consisting of acceleration phases, constant speed phases, and braking phases. These cycles mimic the behavior of an ordinary driver and will allow obtaining the losses that a motor could experience on a daily commute. The latest cycle used is the “Worldwide harmonized Light vehicles Test Procedure” (WLTP) cycle, which will be utilized in the article.

To simulate the behavior of a car as accurately as possible, the motor must be simulated within the architecture of a commercialized vehicle. For this reason, the characteristics of the two vehicles have been implemented in the simulator. These two cars are the “Renault Zoé” and the “Bombardier eCommander”, which will allow testing whether the controls work in two completely different configurations (weight, road quality, etc.).

Finally, throughout the article, the same representation formalism is used. Regardless of the motor and its configuration, the power train will be represented in the same way. The adopted formalism is the Energetic Macroscopic Representation (EMR) [1], which can be used to represent cars, bicycles, or other energy systems. For the different control chains, the Maximum Control Structure (MCS) [2] will be preferred as it works in conjunction with the EMR. Using these two tools will simplify the understanding and operation of the simulated controls.

The first section (Section 2) presents the Energetic Macroscopic Representation used to organize all the different control schemes. The second section (Section 3) exposes the Energetic Macroscopic Representation of an electric vehicle and the Worldwide harmonized Light vehicles Test Procedure (WLTP) cycle. The next two sections present comparative studies of various control schemes for the permanent magnet synchronous motors (Section 4) and for the asynchronous motor (Section 5). Finally, Section 6 draws conclusions.

## 2. Methods and Generic Control Scheme

In order to organize the model and the control of the car, the Energetic Macroscopic Representation (EMR) [1] is used. This is a graphical method that enables the breaking down of the system model into control-oriented components, facilitating the systematic derivation of control schemes. The EMR serves as a roadmap for simplifying the model to create a straightforward vehicle simulation. EMR is used for modeling electrical vehicles [3,4], subway [5], fuel cell [6], wind energy conversion systems [7]. In this paper, several motors and control laws will be evaluated. Then, a generic scheme of the dynamical model and the control process is presented in Figure 1. The orange or yellow blocks represent the plant, i.e., the motor, the batteries, and the environment of the car. The blue blocks stand for the controller (one-speed controller and the specific control block for different motors). All the need blocks in the EMR formalism are presented in detail in the next sections. The parameters and variables of the vehicle are described in Table 1.

Numerical simulations are carried out using the Matlab/Simulink r2011b software.

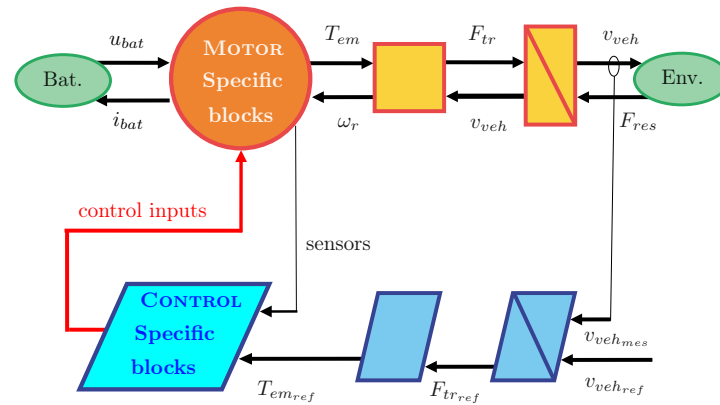


**Figure 1.** Energetic macroscopic representation (EMR) of the electrical vehicle.

**Table 1.** Vehicle parameters and variables.

Parameters	
Name	Meaning
$R_{bat}$ ( $\Omega$ )	Battery internal resistance
$C_{bat}$ (Ah)	Battery capacity
$k_{gbox}$	Gearbox ratio
$r_{wheel}$ (m)	Wheels radius
$M_{veh}$ (kg)	Vehicle mass
$f$	Friction coefficient
$g$ ( $m/s^2$ )	Gravitational acceleration
$\alpha$ ( $^\circ$ )	Angle of the slope
$\rho$ ( $kg/m^3$ )	Density of air
$C_x A$	Drag coefficient
Variables	
Name	Meaning
$u_{bat}$ (V)	Battery voltage
$U_{oc\_bat}(SoC_{bat})$ (V)	Battery open circuit voltage
$SoC_{bat}$ (%)	Battery state of charge
$i_{bat}$ (A)	Battery current
$T_{em}$ (Nm)	Electromagnetic torque
$T_{gbox}$ (Nm)	Gearbox torque
$\omega_r$ (rad/s)	Rotor mechanical speed
$\omega_{gbox}$ (rad/s)	Gearbox speed
$F_{tr}$ (N)	Traction force produce by wheel
$F_{res}$ (N)	Resistance force
$v_{veh}$ (m/s)	Vehicle speed
$v_{wind}$ (m/s)	Wind speed

### 3. Dynamical Model of the Vehicle

This section provides the details of the modeling used for the electric vehicle.

- Batteries are modeled as follows:

$$\begin{cases} u_{bat} = U_{oc\_bat}(SoC_{bat}) - r_{bat}i_{bat} \\ SoC_{bat} = 100\left(1 - \frac{1}{C_{bat}}\right) \int_0^t i_{bat}(\sigma) d\sigma \end{cases} \quad (1)$$

Simulations use battery cells with capacity of 72 Ah and serial resistance of 3.4 m $\Omega$ , 4 cells in parallel, 48 cells in series.

- Gearbox:

$$\begin{cases} T_{gbox} = k_{gbox} T_{em} \\ \omega_r = k_{gbox} \omega_{gbox} \end{cases} \quad (2)$$

In the simulation, the gearbox ratio is adjusted for each engine so that the vehicle can complete the test without the engine exceeding its nominal value (no defluxing).

- Wheels:

$$\begin{cases} F_{tr} = \frac{1}{r_{wheel}} T_{gbox} \\ \omega_{gbox} = \frac{1}{r_{wheel}} v_{veh} \end{cases} \quad (3)$$

- Vehicle body:

$$F_{tr} = M_{veh} \frac{d}{dt} v_{veh} + F_{res} \quad (4)$$

- External environment:

$$F_{res} = f M_{veh} g \cos(\alpha) + 0.5 \rho C_x A (v_{veh} + v_{wind})^2 + M_{veh} g \sin(\alpha) \quad (5)$$

The three control blocks correspond to a speed controller to give reference force needed on the wheel, an inversion of the wheels and gearbox block, and finally, a specific block for the electric motor low-level controller. The speed controller is given by

$$F_{tr_{ref}} = C_{veh}(v_{veh_{ref}} - v_{veh_{mes}}) + F_{res_{mes}} \quad (6)$$

where  $C_{veh}(\cdot)$  is a PI controller. Controller gains are chosen by fixing a second-order dynamic of the vehicle's close loop with  $K_I = M_{veh} \omega_0$  and  $K_P = 2\xi M_{veh} \omega_0$ . Numerical values are  $\xi = 1$  and  $\omega_0 = \frac{2\pi}{T_{res}}$  with  $T_{res} = 2$  s.

Inversion of the wheels relation gives

$$T_{gbox_{ref}} = r_{wheel} F_{tr_{ref}} \quad (7)$$

Inversion of gearbox relation reads

$$T_{em_{ref}} = \frac{1}{k_{gbox}} T_{gbox_{ref}} \quad (8)$$

### 3.1. Speed Cycles

In order to test the vehicle performances in a simulation environment, it is necessary to reproduce driving conditions similar to those of the real world.

The driving cycle WLTP or "Worldwide harmonized Light vehicles Test Procedure" is the new European standard for vehicle testing [8,9]. This cycle is depicted in Figure 2. Since 2018, all new vehicles leaving the factory run through this simulator in order to measure the fuel consumption, exhaust emissions of combustion models, and measure the range of electric vehicles. The cycle has a duration of 1800 s or 30 min and comprises four phases. The first two phases represent an urban cycle, while the last two are extra-urban, with a maximum speed of 131 km/h. The accelerations and decelerations are designed to best represent human behavior.

The resisting force applied to the motor in Figure 1 is given by the external environment formula. Within this formula, three parts can be distinguished.

$$F_{res} = f M_{veh} g \cos(\alpha) + 0.5 \rho C_x A (v_{veh} + v_{wind})^2 + M_{veh} g \sin(\alpha) \quad (9)$$

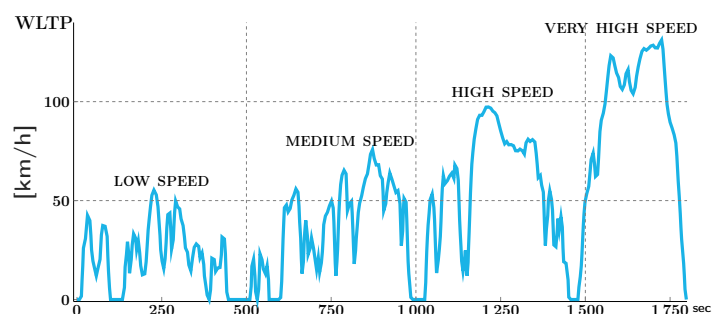


**Figure 2.** Worldwide harmonized Light vehicles Test Procedure (WLTP) cycle.

To begin with, the first part models the rolling force with  $f$  as the rolling resistance coefficient,  $M_{veh}$  as the vehicle mass,  $g$  as the acceleration of gravity ( $9.81 \text{ m/s}^2$ ), and  $\alpha$  as the angle of slope here:  $0 \text{ deg}$ .

Next, the aerodynamic force is the force exerted by air on the moving vehicle. The parameters are  $\rho$  as the density of the air ( $1.204 \text{ kg/m}^3$ ); the variables  $v_{veh}$  and  $v_{wind}$ , respectively, denote the speed of the vehicle and the wind (in the simulation, the wind will be considered zero); and  $SC_x = C_x \times A$  the aerodynamic drag coefficient, which depends on the exposed frontal surface and the shape of the front of the vehicle. The better the air penetration of the vehicle, the smaller the  $SC_x$  coefficient. Finally, the last part of the equation models the force due to the road slope. The sum of the various resisting forces is added to the mass multiplied by the acceleration in the chassis block.

### 3.2. Simulated Vehicles

Two different sets of parameters (see Table 2) are used to faithfully simulate the vehicles in the Figure 3, and are detailed in the following table. The weight of the vehicle indicated does not include the two passengers of 75 kg on board.

The “Renault Zoé” (Figure 3a) is a 100% electric car created for the general public. It is undoubtedly the flagship of the Renault group in the green car sector. Since 2013, the Zoé has been one of the best-selling electric vehicles on the market. This is a city car designed to cover daily commutes, with a range of around 300 km. Its size and weight are therefore relatively small compared with other cars on the market.

The “Bombardier eCommander” (Figure 3b) is an all-terrain vehicle. It can be used for utility or leisure purposes. Its 29” wheels give it solid road holding and the ability to negotiate all kinds of obstacles. Its primary frame, lightweight materials, and limited equipment all help to reduce the weight of the vehicle and hence fuel consumption.

**Table 2.** Simulated vehicle parameters.

Vehicle Specifications	Parameters of Simulated Vehicles	
	Renault Zoé	Bombardier eCommander
$M_{veh}$ (kg)	1502	857
$r_{wheel}$ (m)	0.204 (16")	0.3175 (29")
$f$	0.015 (asphalt)	0.035 (rough road)
$SC_x$	0.75	1.3

The WLTP cycle will be the control comparison tool, the aim being to measure motor losses over a complete or partial cycle and compare these losses with another control for the two presented vehicles.



**Figure 3.** Simulated vehicles: (a) Renault Zoé and (b) Bombardier eCommander.

#### 4. Comparative Study of Different Control Scheme for Permanent Magnet Synchronous Motor

##### 4.1. Modeling of the PMSM

###### 4.1.1. Motor Model

The electrical part of the pmsm is generally modeled as in Figure 4. In order to simplify the three-phase equations, it is necessary to use the classical Park transformation.

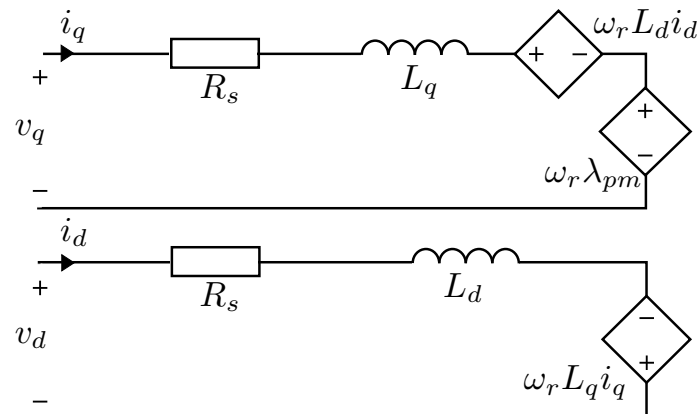


**Figure 4.** PMSM ideal circuits.

The parameters and variables of the PMSM are described in Table 3.

**Table 3.** PMSM parameters and variables.

Parameters	
Name	Signification
$R_s$ ( $\Omega$ )	Stator resistance
$L_d, L_q$ (H)	$d$ and $q$ axis inductances
$\lambda_{pm}$ (Wb)	Permanent magnet flux
$P$	Number of poles
Variables	
Name	Signification
$v_d, v_q$ (V)	$d$ and $q$ axis voltages
$i_d, i_q$ (A)	$d$ and $q$ axis currents
$e_d, e_q$ (V)	Back electromotive forces on $d$ and $q$ axes
$\omega_r$ (rad/s)	Rotor mechanical speed
$T_e$ (Nm)	Electromagnetic torque

The equations of the Permanent Magnet Synchronous Motor are deduced from Figure 4

$$\begin{cases} v_d &= R_s i_d + L_d \frac{di_d}{dt} - \omega_r L_q i_q \\ v_q &= R_s i_q + L_q \frac{di_q}{dt} + \omega_r L_d i_d + \omega_r \lambda_{pm} \end{cases} \quad (10)$$

Equation (10) is expressed in terms of the counter-electromotive forces  $e_d, e_q$

$$\begin{cases} v_d &= R_s i_d + L_d \frac{di_d}{dt} + e_d \\ v_q &= R_s i_q + L_q \frac{di_q}{dt} + e_q \end{cases} \quad (11)$$

The counter-electromotive forces in Equation (11) are described in Equation (12)

$$\begin{cases} e_d &= -\omega_r L_q i_q \\ e_q &= \omega_r (L_d i_d + \lambda_{pm}) \end{cases} \quad (12)$$

Using the right-hand rule, the torque is represented by a vector in the axial direction. It is obtained by calculating the vector product between the fluxes and currents of the  $d, q$  axes. The torque developed by the motor is given by

$$\begin{aligned} T_e &= \frac{3}{2} \frac{P}{2} (\lambda_d i_q - \lambda_q i_d) \\ &= \frac{3}{2} \frac{P}{2} (\lambda_{pm} + (L_d - L_q) i_d) i_q \end{aligned} \quad (13)$$

Because  $\lambda_d = L_d i_d + \lambda_{pm}$  and  $\lambda_q = L_q i_q$  in the rotating synchronous frame.

Two parts can be distinguished within the electromagnetic torque  $T_e$ : the main torque  $T_p = \frac{3}{2} \frac{P}{2} \lambda_{pm} i_q$  and the reluctant torque  $T_r = \frac{3}{2} \frac{P}{2} (L_d - L_q) i_d i_q$  which only appears if  $L_d \neq L_q$ .

#### 4.1.2. Difference between SPMSM and IPMSM

The inductances  $L_d$  and  $L_q$  depend on the motor design. The choice of permanent magnet positioning will influence torque generation. There are two main configurations for the pmsm.

The Surface-Mounted Permanent Magnet Synchronous Motor (SPMSM) (Figure 5a) torque generation is unique in that its permanent magnets are positioned on the outer surface of the rotor. This makes its design fairly straightforward [10]. However, as its magnets are directly exposed to the magnetic field, the stator inductances  $L_d$  and  $L_q$  are similar. It cannot produce reluctant torque.

The Interior Permanent Magnet Synchronous Motor (IPMSM) (Figure 5b) unlike the SPMSM can produce reluctant torque. In a large number of applications, such as position or precision control, reluctance (opposition of the magnetic circuit to a magnetic field) is a parasitic quantity that we seek to suppress. However, in our case (speed control), reluctance can be controlled to obtain a magnetic opposition to our advantage (creating additional torque).

Reluctance appears in the IPMSM because its magnets are integrated into the rotor and can be arranged in a different way [11]. For example, Toyota uses a V-shaped arrangement in its hybrid vehicles. The skewed exposure of the permanent magnets will create a difference between the inductances  $L_d$  and  $L_q$ . This difference is used to create a reluctant torque. The IPMSM will be characterized by its saliency ratio ( $L_q/L_d$ ). The higher this ratio, the greater the torque density. Several techniques exist to increase this ratio: for example, multiplying magnet layers (Figure 6b) or axial laminations (Figure 6c).

Synchronous motor control research will focus exclusively on ipmsm, as loss-reducing controls have more potential.

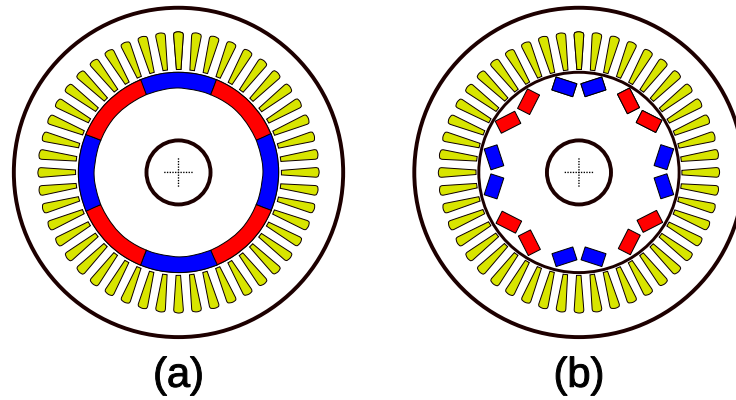


Figure 5. SPMSM (a) vs. IPMSM (b).

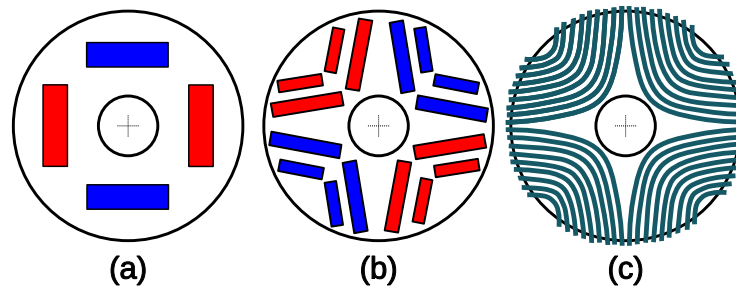


Figure 6. Increasing saliency ratio. (b) multiplying magnet layers with respect to (a). (c) represents axial laminations effect.

#### 4.1.3. Losses Models

The copper losses in Equation (14) are due to the Joule effect caused by the heating of the winding wires. The coefficient  $\frac{3}{2}$  comes from the formula  $P_j = 3RI^2$  in three phases with the stator resistance  $R_s = \frac{R}{2}$  in view of the star configuration.

$$P_{cu} = \frac{3}{2}R_s(i_d^2 + i_q^2) \tag{14}$$

By slightly modifying Figure 4, a model closer to reality can be obtained [12]. Figure 7 adds a resistor representing iron losses within the motor. The currents  $i_d$  and  $i_q$  will now be divided into two parts:  $i_{od}, i_{oq}$  the currents producing the torque; and  $i_{cd}, i_{cq}$  the currents producing the iron losses.

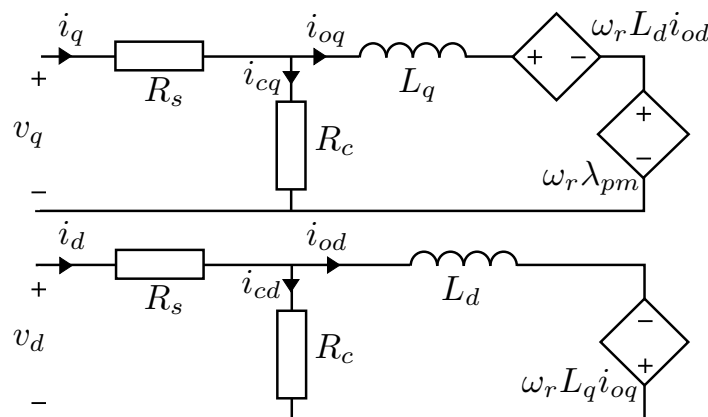


Figure 7. PMSM circuits.

The iron losses are made up of hysteresis and Eddy-current losses. These are losses occurring within the ferromagnetic core, and from [12] iron losses are given by

$$P_{fe} = \frac{3}{2} R_c (i_{cd}^2 + i_{cq}^2) \quad (15)$$

Using the diagram in Figure 7, the values of the currents  $i_{cd}$  and  $i_{cq}$  are deduced in steady state (with respect to the electrical time constant) as follows:

$$\begin{cases} i_{cd} &= -\frac{\omega_r L_q i_{oq}}{R_c} \\ i_{cq} &= \frac{\omega_r (L_d i_{od} + \lambda_{pm})}{R_c} \end{cases} \quad (16)$$

As well as currents  $i_d$  and  $i_q$  with Kirchhoff's current law

$$\begin{cases} i_d &= i_{od} + i_{cd} = i_{od} - \frac{\omega_r L_q i_{oq}}{R_c} \\ i_q &= i_{oq} + i_{cq} = i_{oq} + \frac{\omega_r (L_d i_{od} + \lambda_{pm})}{R_c} \end{cases} \quad (17)$$

This transforms the loss Equations (14) and (15)

$$\begin{aligned} P_{cu} &= \frac{3}{2} R_s \left( \left( i_{od} - \frac{\omega_r L_q i_{oq}}{R_c} \right)^2 + \left( i_{oq} + \frac{\omega_r (\lambda_m + L_d i_{od})}{R_c} \right)^2 \right) \\ P_{fe} &= \frac{3}{2} \left( \frac{(\omega_r L_q i_{oq})^2}{R_c} + \frac{\omega_r^2 (\lambda_m + L_d i_{od})^2}{R_c} \right) \end{aligned} \quad (18)$$

The electromagnetic torque will only be produced by  $i_{od}$  and  $i_{oq}$

$$T_e = \frac{3}{2} \frac{P}{2} (\lambda_{pm} + (L_d - L_q) i_{od}) i_{oq} \quad (19)$$

#### 4.2. EMR of the Permanent Magnet Synchronous Motor

Blocks specific to the IPMSM have been added to the common blocks of Figure 1. These blocks are defined by the following model equations:

- The smoothing coil (to protect the battery from current peaks)

$$u_{bat} - u_{dc} = r_{coil} i_{bat} + L_{coil} \frac{di_{bat}}{dt}$$

- DC bus capacity

$$i_{bat} - i_{dc} = C_{cap} \frac{du_{dc}}{dt}$$

- The inverter or DC/AC converter

$$\begin{cases} \bar{u}_{inv} &= \bar{m}_{inv} u_{dc} \\ I_{dc} &= \bar{m}_{inv} \bar{I}_{em} \end{cases}$$

- Park transformation

$$\begin{cases} u_{dqs} &= P[\theta] \bar{u}_{inv} \\ \bar{I}_{em} &= P[\theta]^{-1} i_{odqs} \end{cases}$$

- $d, q$  armatures

$$u_{dqs} - e_{dqs} = R_s i_{odqs} + \frac{(R_s + R_c) L_{dq}}{R_c} \frac{di_{odqs}}{dt}$$

- Electromagnetic conversion

$$T_{em} = \frac{3}{2} \frac{P}{2} (\lambda_{pm} + (L_d - L_q) i_{ods}) i_{oqs}$$

$$\begin{cases} e_{ds} = -\omega_r L_q i_{oq} \\ e_{qs} = \omega_r (L_d i_{ods} + \lambda_{pm}) \end{cases}$$

Additional parameters and variables are defined in Table 4. Three-phase variables will have the notation  $v\bar{a}r$ .

This gives the EMR of the pull chain from IPMSM to Figure 8. The added blocks are orange.

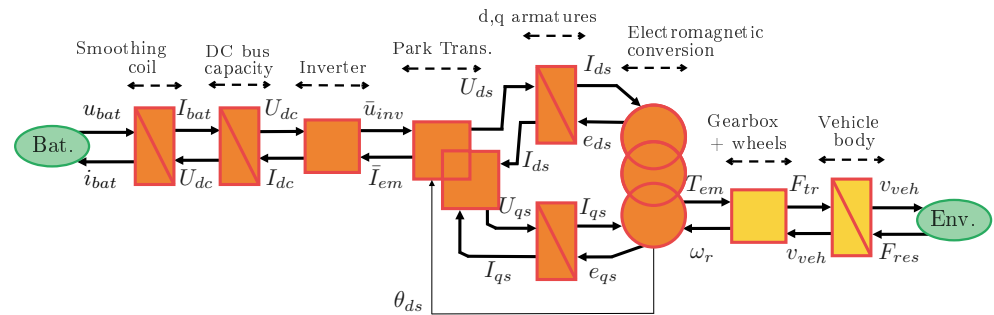


Figure 8. IPMSM vehicle EMR scheme.

Table 4. Supplementary PMSM parameters and variables.

Parameters	
Name	Meaning
$r_{coil}$ ( $\Omega$ )	Coil internal resistance
$L_{coil}$ (H)	Smoothing coil
$C_{cap}$ (H)	Bus capacitor DC
Variables	
Name	Meaning
$u_{dc}$ (V)	DC bus voltage
$\bar{u}_{inv}$ (V)	Three-phase voltages
$I_{dc}$ (A)	DC current
$\bar{I}_{em}$ (A)	Three-phase currents
$\bar{m}_{inv}$	Modulation index

#### 4.3. Parameters of Selected Permanent Magnet Synchronous Motors

Below, Table 5 contains motor parameters found in various articles [13–21]. These motors have power ratings ranging from 40 to 120 kW, corresponding to the power range of an all-terrain quad or an electric city car. Note that the Renault Zoé R135ch  $\approx$  100 kW. We chose to set the value of  $R_c$  to 8  $\Omega$  in order to observe iron losses of the order of 10% of total losses. The goal of our study is not to vary each parameter set individually, but to choose a parameter set large enough to obtain a thorough study.

Table 5. IPMSM motor parameters.

Motor Parameters	Tested Motor Parameters									
	IPMSM 1	IPMSM 6	IPMSM 6.0	IPMSM 7	IPMSM 8	IPMSM 9	IPMSM 10	IPMSM 11	IPMSM 13	IPMSM 14
$P_{nom}$ (kW)	40	100	100	90	118.5	160	100	100	100	150
$T_{nom}$ (Nm)	133	256	256	225	475.6	935	203	203	400	300
$N_{nom}$ (rpm)	2600	3000	3000	2100	2380	1700	4700	4700	1800	5000
$N_{max}$ (rpm)	11,000	12,500	12,500	/	/	/	/	/	3500	/
$U_{dc}$ (V)	240	288	288	360	355.9	700	360	360	230	750
$I_{nom}$ (A)	216	600	600	300	222.7	600	377.5	377.5	/	/
$P$	6	8	8	8	8	8	12	12	8	8
$\lambda_m$ (Wb)	0.07	0.0711	0.0711	0.092	0.213	0.37	0.21	0.04228	0.175	0.095
$L_d$ (mH)	0.375	0.174	0.074	0.59	0.4905	0.43	0.094	0.094	1	0.2
$L_q$ (mH)	0.835	0.292	0.392	2.85	1.3393	0.7	0.153	0.153	1.7	0.55
$R_s$ (mΩ)	29.5	8.2	12	30	6.67	12.1	4.2	4.2	40	10
$R_c$ (Ω)	8	8	8	8	8	8	8	8	8	8
$( L_d - L_q )/\lambda_m$ (mH/Wb)	6.571	1.660	4.473	24.565	3.985	0.730	0.281	1.395	4	3.684

#### 4.4. Control Scheme Comparison

##### 4.4.1. Zdac Control Law

The Zero  $d$ -axis current or ZDAC control is the simplest control applied to PMSM [22]. It allows you to leave the current  $i_d^*$  at zero, so you only need to manage  $i_q^*$  to produce torque. The current  $i_q^*$  comes simply from Equation (19) with  $i_d^* = 0$ , as follows:

$$\begin{cases} i_d^* = 0 \\ i_q^* = \frac{4T_{ref}}{3P\lambda_m} \end{cases} \quad (20)$$

This control law only takes advantage of the production of the main torque. This control seeks to imitate the behavior of an MCC. The following specific blocks have been added (Figure 9). These include the use of a PI corrector and the inverse Park transform. The gains of the PI corrector are computed to impose response time ( $T_{1\%}$ ) of the closed loop:  $K_p = \frac{5L_{d \text{ or } q}}{T_{1\%}}$  and  $K_i = \frac{5R_s}{T_{1\%}}$  with  $T_{1\%} \approx 100$  ms. This gives the Maximum Control Structure (MCS) for ZDAC in Figure 10.

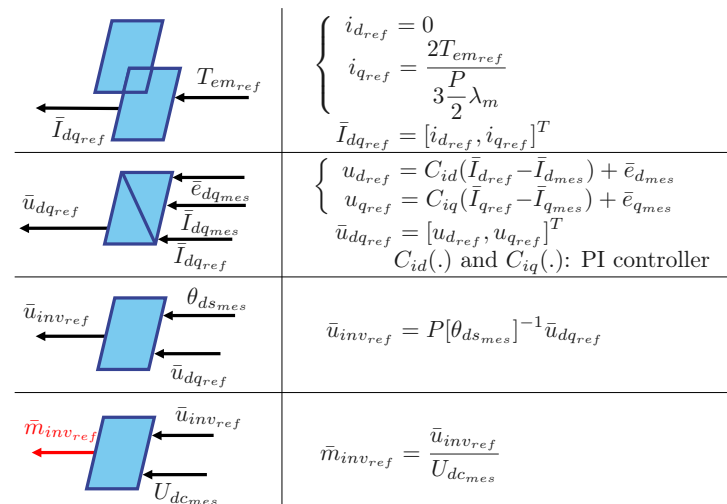


Figure 9. ZDAC control scheme specific blocks.

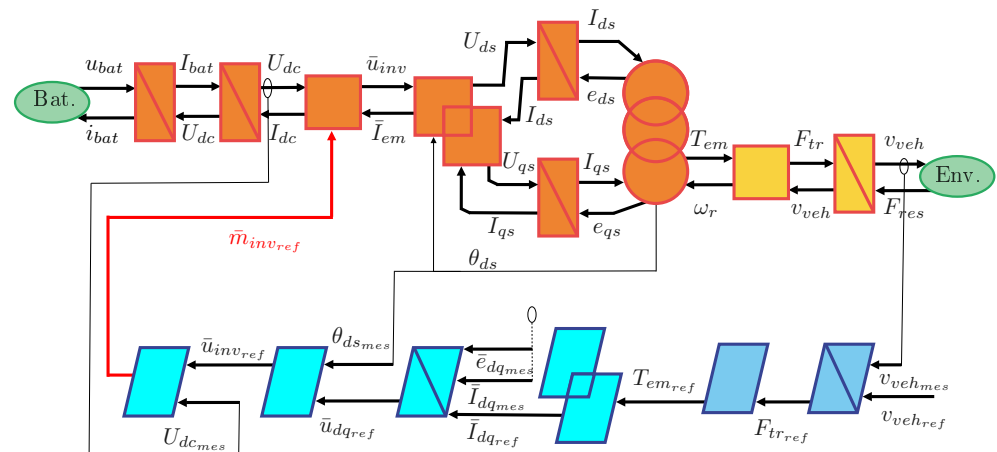


Figure 10. Control structure for ZDAC.

#### 4.4.2. Mtpa Control Scheme

As its name suggests, the Maximum Torque Per Ampere (MTPA) control law attempts to produce the maximum torque produced. By using the reluctant torque of the IPMSM, it will enable the vehicle to achieve good performance by distributing its current more evenly. The current reference  $i_d$  will no longer be fixed at zero but will contribute to torque generation in the same way as  $i_q$ . As copper losses are quadratic, the current distribution between  $i_d$  and  $i_q$  will increase motor efficiency. Knowing that,  $P_{cu} = \frac{3}{2}R_s(i_d^2 + i_q^2)$ . As the total stator current  $i_s = \sqrt{i_d^2 + i_q^2}$ , the losses can be different depending on the distribution between  $i_d$  and  $i_q$  [23]. Note that  $i_d = \alpha i_s$  and  $i_q = (1 - \alpha)i_s$ , then the copper losses become  $P_{cu} = \frac{3}{2}R_s((\alpha i_s)^2 + ((1 - \alpha)i_s)^2) = \frac{3}{2}R_s i_s^2 (2\alpha^2 - 2\alpha + 1)$ . In the interval  $0 < \alpha < 1$ , the minimum is achieved for  $\alpha = 0.5$  and the maxima are located at  $\alpha = 0$  and  $\alpha = 1$ . Loss maxima are therefore when  $i_d = 0$  or  $i_q = 0$ . At first sight,  $i_d = i_q$  is the solution with the lowest losses, but  $i_d$  and  $i_q$  do not produce the same amount of torque. Depending on the motor and profile, the  $\alpha$  coefficient will vary in order to meet the torque of the motor requirements and minimize motor losses. This issue is illustrated in Figure 11, with  $i_s = 100$  A, which can be distributed in different ways. The red dot point ( $i_d = -50$  A,  $i_q = 50$  A) generates fewer losses than the blue dot point ( $i_d = 0$  A,  $i_q = 100$  A) but produces much less torque. The MTPA control attempts to resolve this compromise.

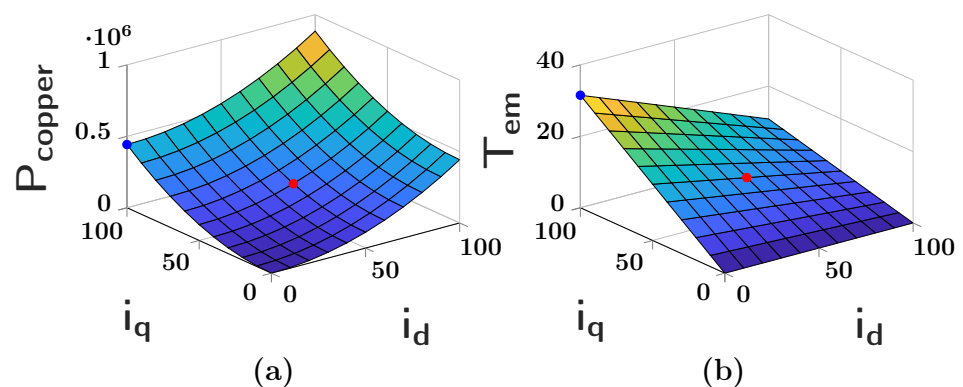


Figure 11. Copper losses (a) and torque generation (b) with respect to current distribution.

The MTPA technique focuses only on suppressing copper losses; iron losses are ignored for the control design ( $R_c = \infty$ ), so  $i_{od} = i_d$  and  $i_{oq} = i_q$  because  $i_{cd} = i_{cq} = 0$  A [24].

We need to solve Equation (21) to find the maximum voltage per ampere

$$\frac{dT_e}{di_d} = 0 \tag{21}$$

The optimal  $i_{d\_ref}$  current is obtained as follows:

$$i_d = \frac{\lambda_{pm}}{2(L_q - L_d)} - \sqrt{\frac{\lambda_{pm}^2}{4(L_q - L_d)^2} + i_q^2} \tag{22}$$

The current  $i_{q\_ref}$  is determined by the following relationship:

$$i_{q\_ref} = \pm \sqrt{i_s^2 - i_{d\_ref}^2} \tag{23}$$

where  $i_s$  is the stator current required by the motor to deliver the required torque. First, check that  $i_s < i_{s\_max}$ , if not, then saturate it at  $i_s = i_{s\_max}$ . The sign of the current  $i_q$  will be the same as that of  $i_s$ . If  $i_s > 0$ , the car is in traction mode. If  $i_s < 0$ , the car is in regenerative braking mode. Note that  $i_s$  and  $T_{em\_ref}$  designate the same thing; the reference input of the block. The two variables are proportional.

The added control blocks are those shown in Figure 9 except for the strategy block, which includes Equations (22) and (23). This gives the maximum MTPA control structure, shown in Figure 12:

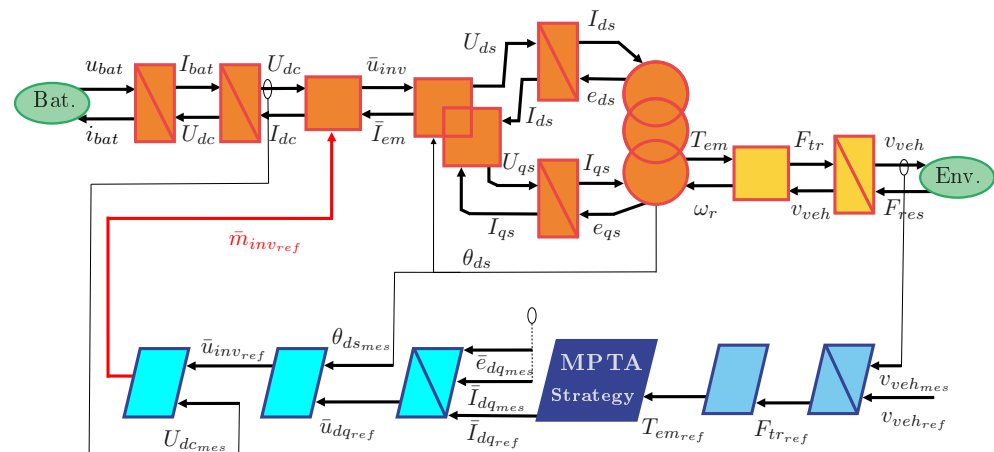


Figure 12. MTPA controller scheme.

#### 4.4.3. Lm/Mtpa Controller

The Losses Minimization/Maximum Torque Per Ampere controller (LM/MTPA) is a hybrid controller combining the MTPA control and the LM control. The choice of which control will prevail over the other is made by adjusting parameter  $\beta$  [12].

The MTPA control previously presented is known to perform well during speed changes and to drastically reduce copper losses, but it does not take into account the iron losses of the motor. The LM control is known to perform less well dynamically but reduces both copper and iron losses. For optimum control, the MTPA control should be used during speed changes and the LM control the rest of the time. This means ignoring iron losses during high torque demand but continuing to take them into account the rest of the time. The  $\beta$  parameter is used to weight the iron losses taken into account. The losses taken into account for the control design are described by Equation (24).

$$P_e = P_{Cu} + \beta P_{Fe} \tag{24}$$

If  $\beta = 1$ , then iron losses are taken into account. The aim is to minimize all motor losses (LM control). If  $\beta = 0$ , only copper losses are taken into account. The aim is to maximize torque per ampere (MTPA control).

To calculate  $\beta$ , we chose the absolute value of the derivative of torque  $T_{em}$ . This is multiplied by a gain of 10 on the nominal torque. The slope of the  $\beta$  must also be saturated and limited. The aim is for the greatest possible torque demand to bring  $\beta$  down to zero. This method replaces the [12] method, which is based on the difference between the reference speed and the measured speed.

To find the optimum trajectory, the mathematical solution is as follows: the losses in Equation (24) are derived with respect to current  $i_{od}$  (torque-producing current on axis  $d$ ) and the roots are found (Equation (25)).

$$\frac{dP_e}{di_{od}} = 0 \tag{25}$$

Once developed, the aim is to make the  $T_{e\_ref}$  pair appear in the Equation (25). This gives an equation to solve of the type (26):

$$\frac{9n_p^2}{4}(R_s R_c^2 i_{od} + \omega_r^2 L_d (R_s + \beta R_c)(L_d i_{od} + \lambda_m))(\lambda_m + (L_d - L_q)i_{od})^3 = T_{e\_ref}^2 (R_s R_c^2 + (R_s + \beta R_c)(\omega_r L_q)^2)(L_d - L_q) \tag{26}$$

The previous equation can be written as follows:

$$AB = T_e^2 C \tag{27}$$

With the following coefficients  $A$ ,  $B$ , and  $C$ :

$$\begin{aligned} A &= \frac{9n_p^2}{4}(R_s R_c^2 i_{od} + \omega_r^2 L_d (R_s + \beta R_c)(L_d i_{od} + \lambda_m)) \\ B &= (\lambda_m + (L_d - L_q)i_{od})^3 \\ C &= (R_s R_c^2 + (R_s + \beta R_c)(\omega_r L_q)^2)(L_d - L_q) \end{aligned}$$

We need to reformulate Equation (27) and find its smallest root, which is the optimal current value  $i_{od}$ . This optimum current will depend on the three inputs  $\omega_r$ ,  $T_{e\_ref}$ , and  $\beta$ . Next, use Equation (19) to find  $i_{oq}$  and Equation (17) to obtain  $i_{d\_ref}$  and  $i_{q\_ref}$ .

The control blocks added are those shown in Figure 9, except for the strategy block LM/MTPA, which uses Equation (27), and the "strategy  $\beta$ " block, which uses the scheme (Figure 13). This gives the Maximum Control Structure (MCS) for LM/MTPA, shown in Figure 14.

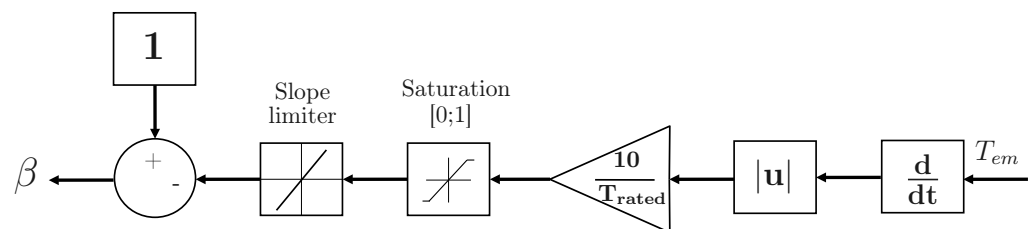


Figure 13. Calculation of  $\beta$ .



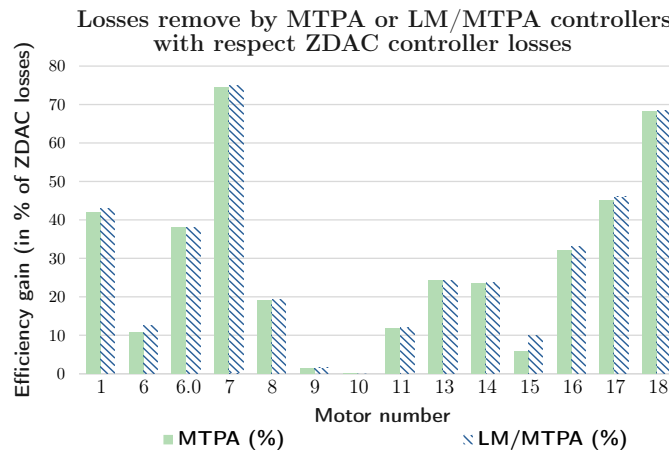


Figure 15. Comparison of regained losses with respect to ZDAC control.

Table 7. Parameters for IPMSM motor.

Motor Parameters				
Motor Parameters	IPMSM 15	IPMSM 16	IPMSM 17	IPMSM 18
$P_{nom}$ (kW)	150	40	40	90
$T_{nom}$ (Nm)	300	133	133	225
$N_{nom}$ (rpm)	5000	2600	2600	2100
$N_{max}$ (rpm)	/	11,000	11,000	/
$U_{dc}$ (V)	750	240	240	360
$I_{nom}$ (A)	/	216	216	300
$P$	8	6	6	8
$\lambda_m$ (Wb)	0.15	0.0835	0.075	0.13
$L_d$ (mH)	0.2	0.375	0.3	1
$L_q$ (mH)	0.575	0.835	0.9	3
$R_s$ (mΩ)	10	29.5	29.5	30
$R_c$ (Ω)	20	20	20	20
$(L_d - L_q)/\lambda_m$	2.5	5.5	8.0	15.385

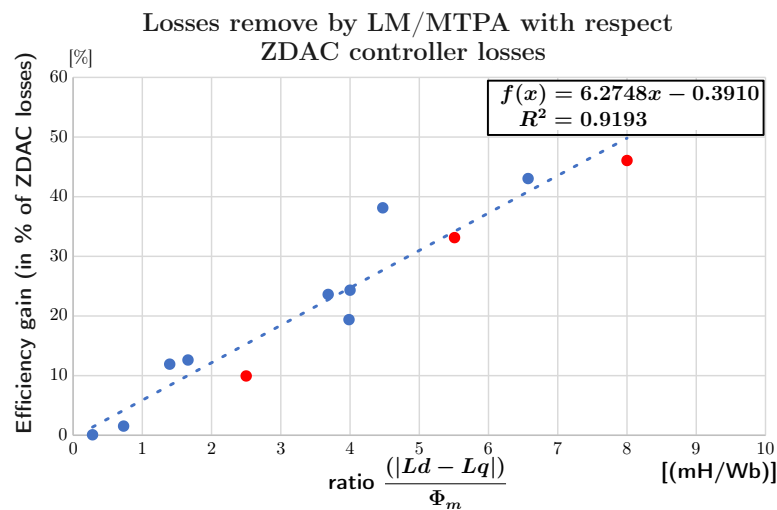


Figure 16. Losses removed as a function of the ratio  $(|L_d - L_q|)/\lambda_m$ —Linear zone. Blue dot correspond to first motors serie in Table 5, red dot correspond to additional simulated motor in Table 7, dotted line is the trend line.

Table 8 shows the yields of the best and worst control on each motor. Gross efficiencies depend largely on the value of the stator resistance  $R_s$  and the amplitude of the circulating currents (Equation (34)). The higher the value, the lower the motor efficiency. But, the higher  $R_s$ , the more effective the MTPA strategy will be (greater efficiency difference). In the same way as the ratio  $(L_d - L_q)/\lambda_m$ , the value of  $R_s$  can be interesting to analyze in order to anticipate losses that can be eliminated before implementing the control on a motor.

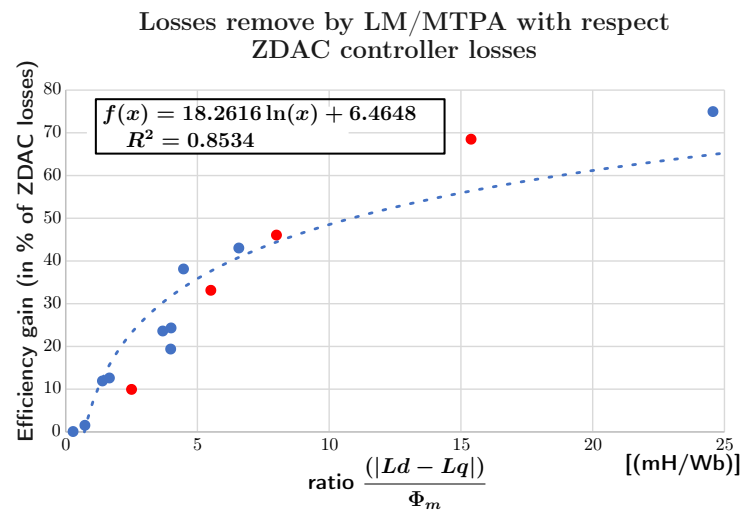


Figure 17. Losses deleted based on the ratio  $(|L_d - L_q|) / \lambda_m$ —extended area.

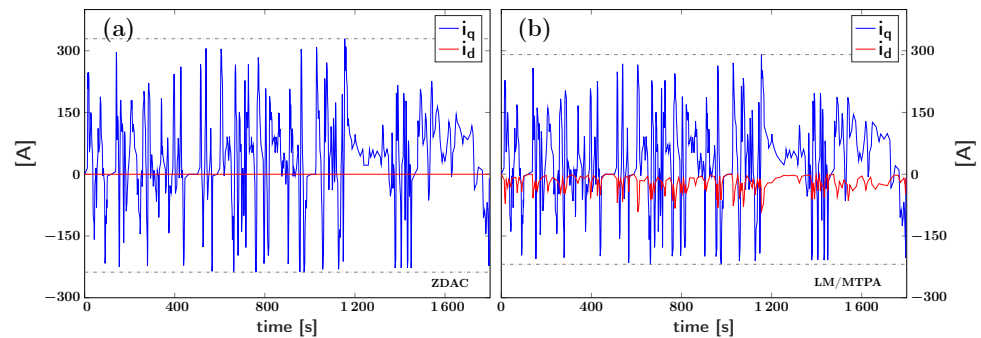


Figure 18. Current distribution comparison: (a) ZDAC—(b) LM/MTPA.

Table 8. Comparison of energy efficiency.

Motor Name	Efficiency of the Least Efficient Control (ZDAC)	Efficiency of the Most Efficient Control (LM/MTPA)	Efficiency Difference
IPMSM1	81.5%	88.6%	+7.1%
IPMSM6	95.7%	96.2%	+0.5%
IPMSM6.0	91.5%	94.5%	+3%
IPMSM7	82.1%	94.8%	+12.7%
IPMSM8	97.3%	97.8%	+0.5%
IPMSM9	96.8%	96.9%	+0.1%
IPMSM10	94.7%	94.7%	+0%
IPMSM11	97.9%	98.1%	+0.2%
IPMSM13	88.7%	91.2%	+2.5%
IPMSM14	96.2%	97.1%	+0.9%

In conclusion, the MTPA and LM/MTPA controls make it possible to eliminate a significant proportion of losses by using reluctant torque in addition to the main torque. Their simplicity of installation makes them easy to integrate into motors coming out of the industry or already on the road. In addition, as motors age, stator resistance tends to increase slightly, so the losses eliminated by these two controls will become more expensive. The choice between MTPA and LM/MTPA is in the hands of the expert. Indeed, in the above case, the difference is not obvious, but if the voltage and frequency of the supply increase, a discrepancy will be created. Finally, detecting a link between suppressed losses and the ratio of main torque to reluctant torque enables us to predict the gains to be made by implementing these controls. A reading of the motor parameters can indicate the relevance or otherwise of changing standard control by these improved controls.

### 5. Comparative Study of Different Control Scheme for Asynchronous Motor

#### 5.1. Modeling

##### 5.1.1. Asynchronous Motor Model

The basic principle of the asynchronous motor may be similar to that of the PMSM, but there are some major differences. The rotor of the asynchronous machine has no permanent magnets, but a cage with iron bars (squirrel cage). The stator field created will sweep across the rotor bars, causing currents to flow in the same direction. This is due to the phenomenon of induction: the stator will induce currents in the rotor bars that would otherwise not need to be energized. The rotor will not reach synchronous speed, and there will always be an offset, known as slip. Asynchronous motor variables and parameters are given in Table 9. The equivalent phase diagrams of the asynchronous motor are shown in Figure 19.

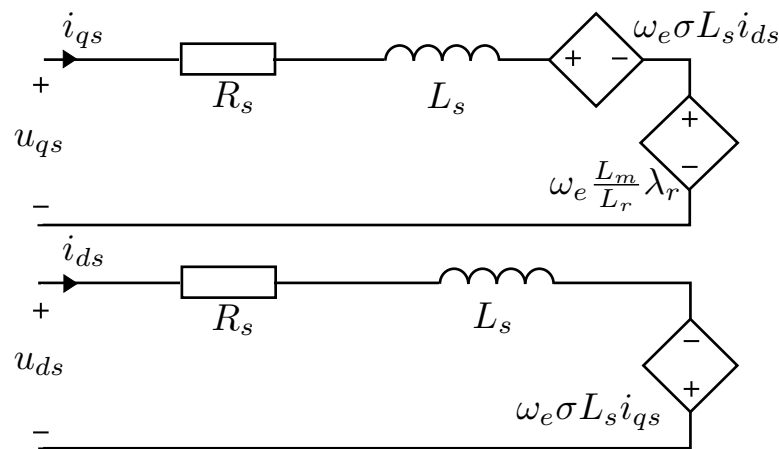


Figure 19. Asynchronous motor wiring diagrams.

Table 9. Asynchronous motor variables and parameters.

Parameters	
Name	Meaning
$R_s$ ( $\Omega$ )	Stator resistance
$R_r$ ( $\Omega$ )	Rotor resistance
$L_s$ (H)	Stator inductance
$L_r$ (H)	Rotor inductance
$L_m$ (H)	Mutual inductance
$P$	Number of poles
$K_H$	Hysteresis loss coefficient
$K_e$	Coefficient of Eddy current losses
Variables	
Name	Meaning
$u_{dqs}$ (V)	$d$ and $q$ axis tensions
$i_{dqs}$ (A)	$d$ and $q$ axis currents
$e_{dqs}$ (V)	Counter-electromotive forces of axes $d$ and $q$
$\omega_e$ (rad/s)	Synchronization speed
$\omega_r$ (rad/s)	Rotor speed
$\omega_{slip}$ (rad/s)	Slip speed
$\lambda_r$ (Wb)	Rotor flux
$\lambda_m$ (Wb)	Mutual flux
$T_e$ (rad/s)	Motor torque

The equations of the asynchronous motor are described below. As with the PMSM, we need to go through the Park transformation. Equations (28)–(32) are taken from [25]. The stator voltages of the  $d$  and  $q$  armatures

$$\begin{cases} u_{ds} = R_s i_{ds} + \sigma L_s \frac{d}{dt} i_{ds} + e_{ds} \\ u_{qs} = R_s i_{qs} + \sigma L_s \frac{d}{dt} i_{qs} + e_{qs} \end{cases} \quad (28)$$

Pseudo counter-electromotive forces, as follows:

$$\begin{cases} e_{ds} &= -\omega_e \sigma L_s i_{qs} \\ e_{qs} &= \omega_e \sigma L_s i_{ds} + \omega_e \frac{L_m}{L_r} \lambda_r \end{cases} \quad (29)$$

With  $\sigma = 1 - \frac{L_m^2}{L_s L_r}$  and  $\omega_e = \frac{P}{2} \omega_r + \omega_{slip} = \frac{P}{2} \omega_r + \frac{R_r}{L_r} \frac{L_m}{\lambda_{dr}} i_{qs}$ . The torque formula follows the same principle as Equation (13), as follows:

$$T_e = \frac{3}{2} \frac{P}{2} \frac{L_m}{L_r} [\lambda_{dr} i_{qs} - \lambda_{qr} i_{ds}] \quad (30)$$

The rotor magnetization below clearly shows that the flux inside the motor is dependent on  $i_{ds}$ , as follows:

$$L_m i_{ds} = \lambda_r + \frac{L_r}{R_r} \frac{d}{dt} \lambda_r \quad (31)$$

Now, we choose the orientation of the reference frame so as to have  $\lambda_{dr} = \lambda_r$  and  $\lambda_{qr} = 0$ . The torque formula thus becomes

$$T_e = \frac{3}{2} \frac{P}{2} \frac{L_m}{L_r} \lambda_{dr} i_{qs} = \frac{3P}{4} \frac{L_m^2}{L_r} \frac{1}{\frac{L_r}{R_r} + 1} i_{ds} i_{qs} \quad (32)$$

And this gives in steady state

$$T_e = \frac{3P}{4} \frac{L_m^2}{L_r} i_{ds} i_{qs} \quad (33)$$

### 5.1.2. Losses Model

The loss model below is taken from the articles [26–28]. Copper losses represent Joule effect losses in the stator and rotor, as follows:

$$P_{COPPER} = \frac{3}{2} [R_s (i_{qs}^2 + i_{ds}^2) + R_r (i_{qr}^2 + i_{dr}^2)] = \frac{3}{2} [R_s (i_{qs}^2 + i_{ds}^2) + R_r i_{qr}^2] \quad (34)$$

Here, the current  $i_{dr}$  is zero because according to the rotor voltage formula  $u_{dr} = R_r i_{dr} + \frac{d}{dt} \lambda_{qr} - (\omega_s - \omega_r) \lambda_{qr} = 0$  and  $\lambda_{qr} = 0$ .

Iron losses are composed of hysteresis and Eddy current losses

$$P_{IRON} = P_{hys} + P_{eddy} = K_H \omega_e \lambda_m^2 + K_e \omega_e^2 \lambda_m^2 \quad (35)$$

where  $\lambda_m^2 = \lambda_r^2 + \lambda_s^2 = L_m^2 \frac{L_{lr}^2}{L_r^2} i_{qs}^2 + L_m^2 i_{ds}^2$ .

### 5.2. EMR of Asynchronous Motors

The blocks specific to the Asynchronous Motor drive train are given by the following expression:

- Rotor magnetization

$$L_m i_{ds} = \lambda_{dr} + \frac{L_r}{R_r} \frac{d}{dt} \lambda_{dr}$$

- Electromagnetic conversion

$$T_{em} = \frac{3}{2} \frac{P}{2} \frac{L_m}{L_r} (\lambda_{dr} i_{qs} + \lambda_{qr} i_{ds})$$

$$\begin{cases} e_{ds} = -\omega_{d/s} \left(1 - \frac{L_m^2}{L_s L_r}\right) L_s i_{qs} \\ e_{qs} = \omega_{d/s} \left(1 - \frac{L_m^2}{L_s L_r}\right) L_s i_{ds} + \omega_{d/s} \frac{L_m}{L_r} \lambda_{dr} \end{cases}$$

$$\theta_{d/s} = \int \frac{P}{2} \Omega_r + \frac{R_r L_m}{L_r \lambda_{dr}} i_{qs} dt$$

The EMR of the asynchronous motor vehicle is given on Figure 20 (by reusing common blocks of Figures 1 and 8).

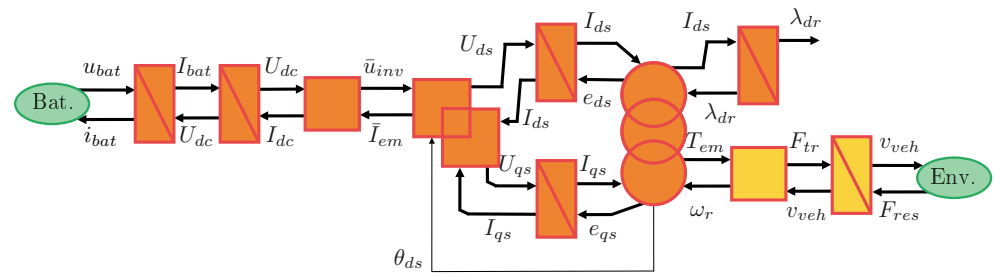


Figure 20. Energetic macroscopic representation of a vehicle with asynchronous motor.

### 5.3. Parameters of Selected Asynchronous Motors

Table 10 containing the motor parameters taken from the article [29]. These motors range in power from 37.5 to 160 kW, corresponding to the power range of an electric city car (Renault Zoé R135ch ≈ 100 kW).

Table 10. Asynchronous Motor parameters.

Motor Parameters	Motor Parameters									
	MAS_4	MAS_5	MAS_6	MAS_7	MAS_12	MAS_13	MAS_17	MAS_18	MAS_19	MAS_20
$P_{nom}$ (kW)	37	74.5	111	149	74.5	111	37	75	110	160
$T_{nom}$ (Nm)	192	507.5	497.5	865	533	507.5	242.5	475.1	661	1055
$N_{nom}$ (rpm)	1780	1780	1785	1785	1780	1785	1480	1484	1487	1487
$U_{dc}$ (V)	460	460	460	460	575	575	400	400	400	400
$I_{nom}$ (A)	54	135.7	140.6	229.6	113	116	65	124.4	173.5	270
$f$ (Hz)	60	60	60	60	60	60	50	50	50	50
$P$	4	4	4	4	4	4	4	4	4	4
$R_s$ (mΩ)	99.6	39.5	30.2	18.1	59.6	45.8	82.3	35.5	21.5	13.7
$R_r$ (mΩ)	58.37	22.15	17.21	9.956	32.81	26.34	50.3	20.92	12.31	7.728
$X_m$ (Ω)	11.457	6.273	4.128	3.55	10.34	6.03	8.52	4.74	3.26	2.42
$X_{sd} = X_{rd}$ (mΩ)	326.8	146.6	106.6	71.6	238.6	159.8	227.4	105.2	71	47.7
$L_m$ (mH)	30.39	16.64	10.95	9.42	27.42	15.99	27.11	15.1	10.38	7.69
$L_s$ (mH)	31.258	17.03	11.233	9.61	28.05	16.41	27.83	15.44	10.61	7.84
$L_r$ (mH)	31.576	17.029	11.2329	9.605	28.053	16.414	27.8344	15.435	10.606	7.8418
$L_{ls}$ (mH)	0.867	0.389	0.283	0.190	0.633	0.424	0.724	0.335	0.226	0.152
$L_{lr}$ (mH)	0.867	0.389	0.283	0.190	0.633	0.424	0.724	0.335	0.226	0.152

### 5.4. Controller Comparison

#### 5.4.1. Field-Oriented Control (FOC)

The aim of field-oriented control is to decouple flux and torque. The first step is to set the nominal flux at a constant value. The relationship (31) ensures that the reference current  $i_{ds\_ref}$  remains at a constant value. Nominal flux is usually calculated using the formula  $\phi_{nom} = L_m \times i_{d\_nom}$ . This formula was not used, as the current  $i_{d\_nom}$  is calculated from tests on the motor at no load. Another formula simulating this behavior was preferred, as follows:

$$\phi_{nom} = \frac{u_{dc\_ref} - 400 R_s}{2\pi f_{nom}} \quad (36)$$

The reference flux ( $\lambda_{dr}$ ) used in our simulation comes from Formula (37).

$$\lambda_{dr} = \frac{1}{\frac{L_r}{R_r} s + 1} \times \phi_{nom} \times \left( \frac{u_{dc\_mes}}{u_{dc\_ref}} \right) \tag{37}$$

On the other axis, the current  $i_{q\_ref}$  ensures that torque demand is met by returning the torque in Equation (30). The aim is for the torque of the asynchronous motor to depend on a single current, as in a DC motor. This equation is detailed and linked to the blocks on Figure 21.

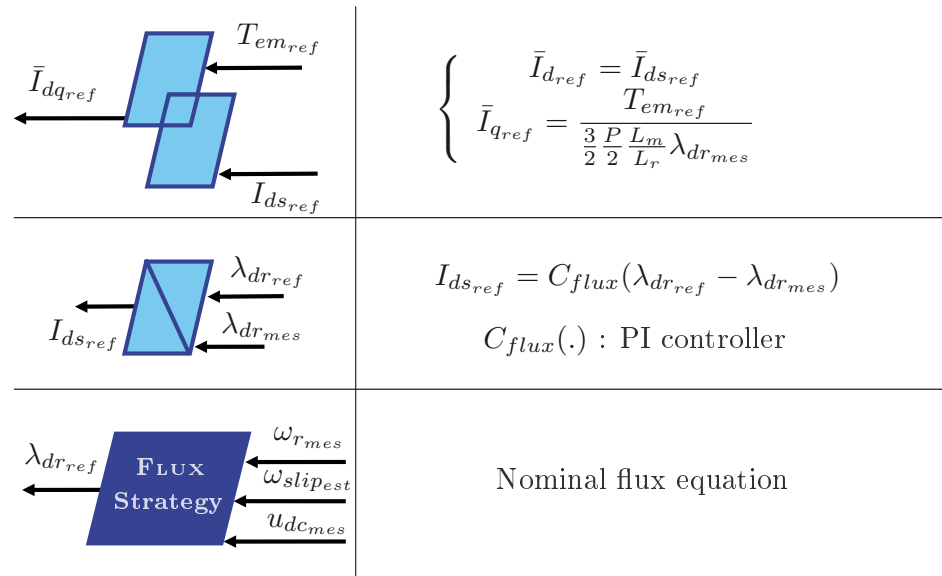


Figure 21. Specific MAS FOC blocks.

Figure 22 shows the complete representation of the FOC scheme.

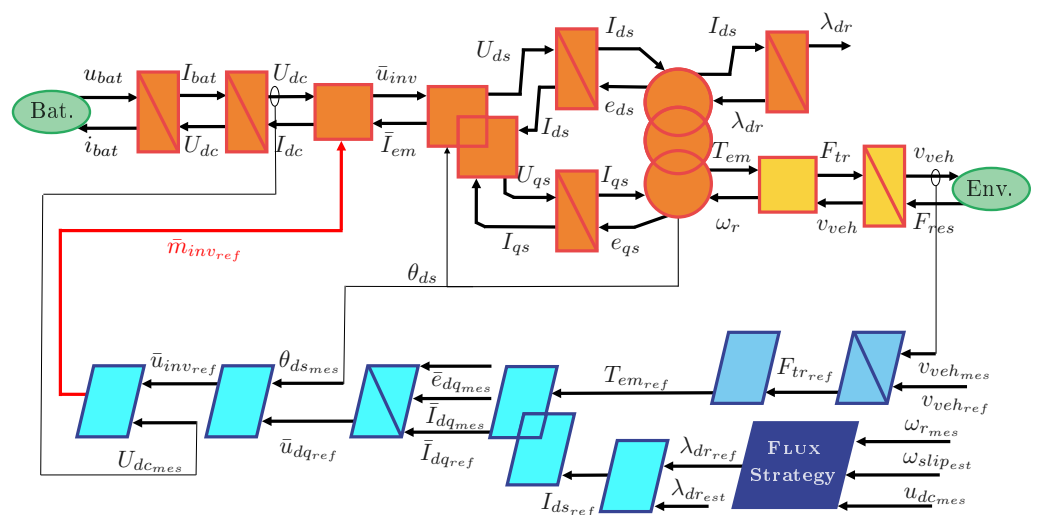


Figure 22. EMR asynchronous motor FOC.

#### 5.4.2. Optimized Flux Control n°1

The aim of the Optimized Flux Control n°1, 2, and 3 is to modulate the flux ( $\lambda_{ref}$ ) instead of leaving it constant. Indeed, the FOC method keeps a constant medium-high flux regardless of torque demand, in order to simplify its implementation. This constant flux results in the permanent circulation of a  $i_{ds}$  current, which in turn generates copper and iron losses.

The main problem with the FOC control is, why leave  $i_{ds}$  at a high value when there is no torque demand? The way to reduce losses is to leave  $i_{ds}$  at zero or close to zero when there is no torque demand and to find the best combination between  $i_{ds}$  and  $i_{qs}$  when torque demand occurs. Indexing the current to torque demand would not only meet dynamic requirements quickly, but also reduce current-related losses  $i_{ds}$  when the profile is smooth.

The first method (Opt\_flux\_1) comes from the article [26] published in 2021, this method seeks the optimal flux to cause the minimum losses. Since the optimal flux  $\lambda_{dr}$  and current  $i_{ds}$  are very closely related, finding the optimal flux and current amounts to the same thing. The article begins its reasoning by looking for the steady-state torque (Equation (33)) in Equation (34), the loss model becomes

- Copper losses:

$$P_{COPPER} = \frac{3}{2} \left[ R_s \left( \frac{16}{P^2} \frac{T_e^2}{k_T^2 \lambda_r^2} + \frac{\lambda_r^2}{L_m^2} \right) + R_r \frac{L_m^2}{L_r^2} \left( \frac{16}{P^2} \frac{T_e^2}{k_T^2 \lambda_r^2} \right) \right] \quad (38)$$

with  $k_T = \frac{3L_m}{L_r}$ .

- Iron losses:

$$P_{IRON} = (K_H \omega_e + K_e \omega_e^2) \left( \frac{16}{P^2} \frac{L_m^2 L_r^2}{L_r^2} \frac{T_e^2}{k_T^2 \lambda_r^2} + \lambda_r^2 \right) \quad (39)$$

Total losses:

$$P_{LOSSES} = P_{COPPER} + P_{IRON} \quad (40)$$

In order to obtain the flux with the lowest losses, we need to derive the total losses with respect to  $\lambda_r$  and find the smallest root:  $\frac{dP_{LOSSES}}{d\lambda_r} = 0$ . Inserting (38) and (39) into the previous equation gives

$$\frac{d \left( \frac{3}{2} \left[ R_s \left( \frac{16}{P^2} \frac{T_e^2}{k_T^2 \lambda_r^2} + \frac{\lambda_r^2}{L_m^2} \right) + R_r \frac{L_m^2}{L_r^2} \left( \frac{16}{P^2} \frac{T_e^2}{k_T^2 \lambda_r^2} \right) \right] + (K_H \omega_e + K_e \omega_e^2) \left( \frac{16}{P^2} \frac{L_m^2 L_r^2}{L_r^2} \frac{T_e^2}{k_T^2 \lambda_r^2} + \lambda_r^2 \right) \right)}{d\lambda_r} = 0 \quad (41)$$

The expression  $(K_H \omega_e + K_e \omega_e^2)$  is simplified within an equivalent resistor  $R_f$ . By isolating  $\lambda_r$  on one side, we obtain the equation

$$\lambda_{opt}^4 = \frac{\frac{T_e^2}{k_T^2} \frac{16}{P^2} \left( \frac{3}{2} \left( R_s + \frac{R_r L_m^2}{L_r^2} \right) + R_f \left( \frac{L_m^2 L_r^2}{L_r^2} \right) \right)}{R_f + \frac{3}{2} \frac{R_s}{L_m^2}} \quad (42)$$

The optimal flux is therefore

$$\lambda_{opt} = \sqrt{\frac{4}{k_T P} \sqrt{\left( \frac{\frac{3}{2} \left( R_s + \frac{R_r L_m^2}{L_r^2} \right) + R_f \left( \frac{L_m^2 L_r^2}{L_r^2} \right)}{R_f + \frac{3}{2} \frac{R_s}{L_m^2}} \right)} \sqrt{T_e}} \quad (43)$$

The maximum structure for optimal flux control is added to the EMR in Figure 23. The added blocks are similar to the FOC except for the strategy block, which contains Equation (43).

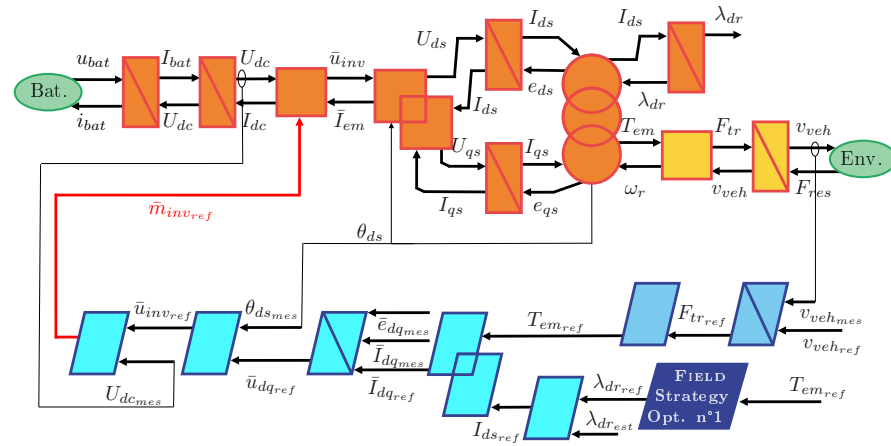


Figure 23. EMR control structure for Optimized Flux Control n°1.

### 5.4.3. Optimized Flux Control n°2

The second method (Opt\_flux\_2) comes from the article [27], published in 2022. The principle is similar, but the model is slightly different and the method changes, as optimal currents are calculated immediately. Here, the flux is not used directly. Based on the loss model in the article, the following equation appears:

$$P_{loss} = P_{scu} + P_{rcu} + P_{fe} = (i_{ds}^2 + i_{qs}^2)R_s + (i_{dr}^2 + i_{qr}^2)R_r + \frac{(V_{md}^2 + V_{mq}^2)}{R_{fe}} \quad (44)$$

With the magnetizing voltages of the  $d$  and  $q$  branches representing the coupling between the voltages and currents of the  $d$  and  $q$  axes,

$$\begin{aligned} V_{md} &= -\omega_e \frac{L_m L_{lr}}{L_r} i_{qs} \\ V_{mq} &= -\omega_e L_m i_{ds} \end{aligned} \quad (45)$$

Inserting Equation (45) into Equation (44) gives

$$P_{loss} = (R_s + \frac{\omega_e^2 L_m^2}{R_{fe}}) i_{ds}^2 + (R_s + \frac{R_r L_m^2}{L_r^2} + \frac{\omega_e^2 L_m^2 L_{lr}^2}{R_{fe} L_r^2}) i_{qs}^2 = R_d(\omega_e) i_{ds}^2 + R_q(\omega_e) i_{qs}^2 \quad (46)$$

where functions  $R_d(\omega_e)$  and  $R_q(\omega_e)$  are defined by  $R_d(\omega_e) = R_s + \frac{\omega_e^2 L_m^2}{R_{fe}}$ ,  $R_q(\omega_e) = R_s + \frac{R_r L_m^2}{L_r^2} + \frac{\omega_e^2 L_m^2 L_{lr}^2}{R_{fe} L_r^2}$  et  $m_1 = \frac{3P}{4} \frac{L_m}{L_r}$ .

Unlike the Optimized Flux Control n°1, we derive the total losses with respect to the current  $i_{ds}$  to obtain the minimum losses.

$$\frac{dP_{loss}}{di_{ds}} = 2i_{ds}R_d(\omega_e) + 2i_{qs}R_q(\omega_e) \frac{di_{qs}}{di_{ds}} = 0 \quad (47)$$

Or

$$2i_{ds}R_d(\omega_e) + 2R_q(\omega_e) \left( \frac{i_{qs}}{i_{ds}} \right) = 0 \quad (48)$$

The blocks of the control chain are similar to the previous ones except for the strategy block, which includes the following equations:

$$\begin{aligned} i_{ds\_opt} &= \sqrt{\frac{R_q(\omega_e)}{R_d(\omega_e)} i_{qs}} \\ i_{qs\_opt} &= \sqrt{\frac{T_{em}^{ref} R_q(\omega_e)}{m_1 R_d(\omega_e)}} \\ \lambda_r^{ref} &= L_m i_{ds\_opt} \end{aligned} \quad (49)$$

Assembling the traction chain and control blocks gives the complete EMR diagram (Figure 24).

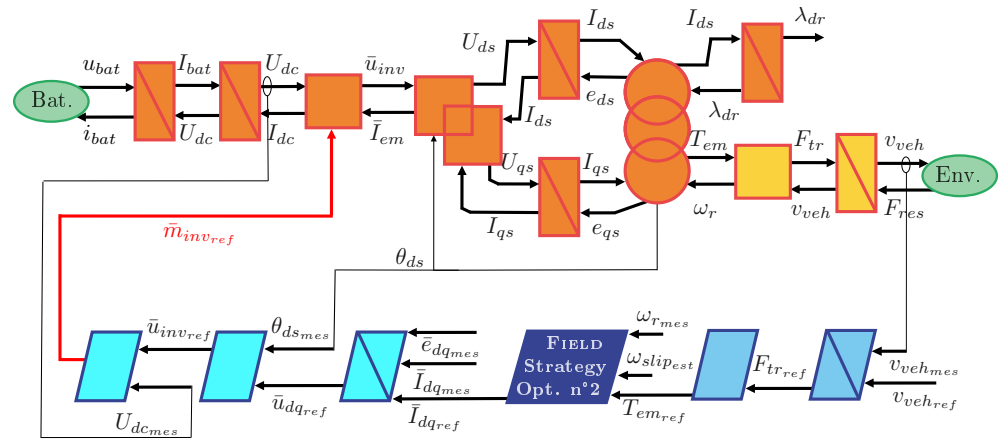


Figure 24. EMR control structure for Optimized Flux Control n°2.

#### 5.4.4. Optimized Flux Control n°3

The last method (Opt\_flux\_3) comes from the article [28], published in 2023. In the same way, the starting point is the loss model of the motor, and the aim is to minimize total losses by deriving them with respect to current  $i_{ds}$ . The current  $i_{ds\_opt}$  is given by the following equation:

$$i_{ds\_opt} = \sqrt[4]{\frac{B}{A} \left( \frac{T_e}{k} \right)^2} \quad (50)$$

With the following coefficients  $A$ ,  $B$ , and  $C$ :

$$A = R_s + (K_h \omega_e + K_e \omega_e^2) L_m^2$$

$$B = R_s + R_r \frac{L_m^2}{L_r^2} + (K_h \omega_e + K_e \omega_e^2) \frac{L_m^2}{L_r^2} ((L_r - L_m)^2)$$

$$C = \frac{3}{2} \frac{P}{2} \frac{L_m^2}{L_r}$$

The difference here is that iron losses have not been simplified within an iron resistor  $R_{fe}$ . This gives the complete EMR diagram (Figure 25).

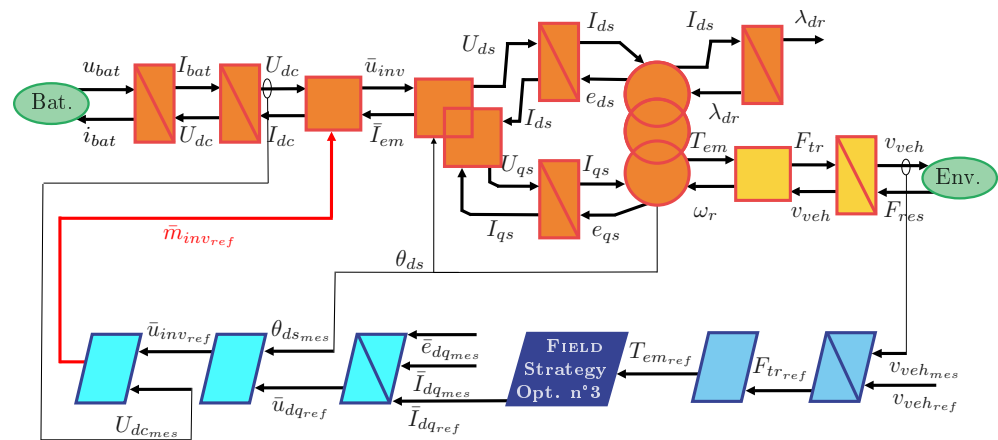


Figure 25. EMR control structure for Optimized Flux Control n°3.

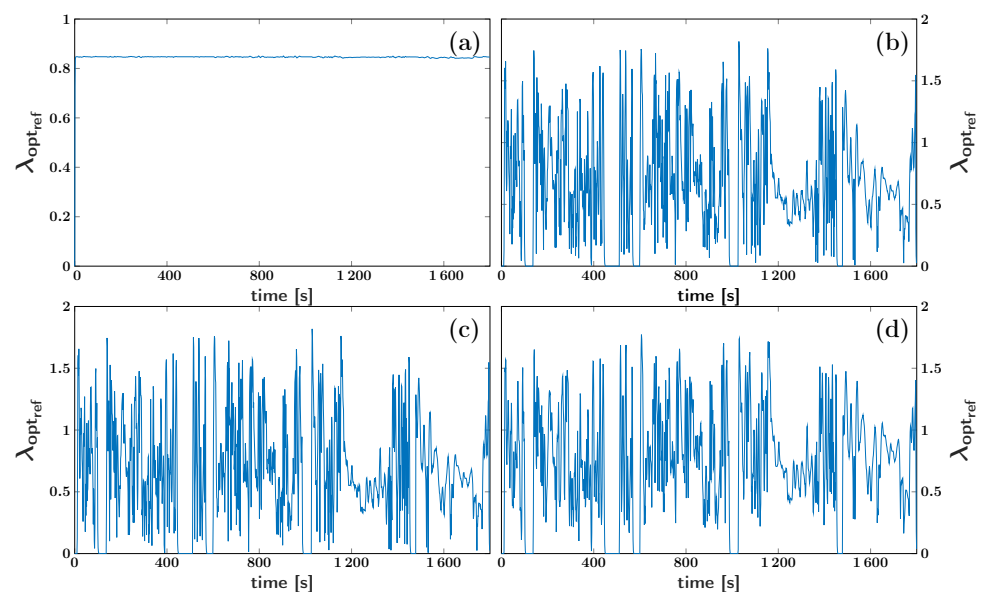
### 5.4.5. Results

The Table 11 below gathers the loss results of the four previous control scheme after a complete cycle. The aim is to reach the same operating region as for IPMSM. With the exception of the MAS4 and MAS17 (less powerful), which are simulated with Bombardier architecture, all other vehicles are simulated with Zoé architecture.

**Table 11.** Table of results for FOC, Opt\_flux\_1, Opt\_flux\_2, and Opt\_flux\_3 control scheme.

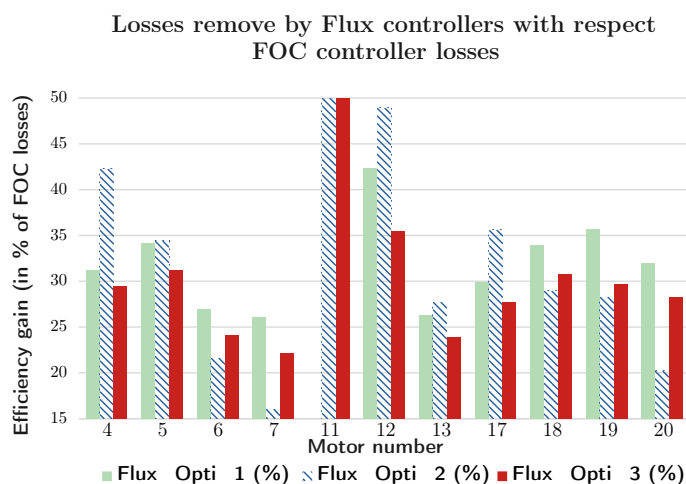
Motor Name	Cycle	Parameters		FOC Controller		Opt_Flux_1 Controller		Opt_Flux_2 Controller		Opt_Flux_3 Controller	
		Duration	Energy Expended (Wh)	Lost Energy (Wh)	Lost Energy (Wh)	Losses Deleted (%)	Lost Energy (Wh)	Losses Deleted (%)	Lost Energy (Wh)	Losses Deleted (%)	
MAS4	0.9 × WLTP	1000 s	1144	77.7	53.4	31.2	44.9	42.3	54.8	29.4	
MAS5	WLTP	1400 s	2854	157.4	103.6	34.2	103.3	34.4	108.3	31.2	
MAS6	WLTP	1400 s	2854	157.6	115.1	27	123.6	21.6	119.7	24.1	
MAS7	WLTP	1800 s	4740	200.4	148.1	26.1	168.4	16	156	22.2	
MAS12	WLTP	1800 s	4740	290.7	167.5	42.4	148.4	48.9	187.5	35.5	
MAS13	WLTP	1800 s	4740	258.4	190.4	26.3	186.9	27.7	196.7	23.9	
MAS17	0.9 × WLTP	1000 s	1144	78.9	55.3	29.9	50.8	35.6	57	27.8	
MAS18	WLTP	1400 s	2854	174.9	115.1	34	124.3	29	121.1	30.1	
MAS19	WLTP	1800 s	4740	248.9	160.1	35.7	178.6	28.3	208.3	16.3	
MAS20	WLTP	1800 s	4740	201.0	136.7	32	160.3	20.2	144.3	28.2	

Figure 26 shows the evolution of flux as a function of time. The three strategies applied are similar, but with a few differences that appear according to motor speed.



**Figure 26.** Flux comparison: (a) FOC—(b) Flux\_Opti\_1—(c) Flux\_Opti\_2—(d) Flux\_Opti\_3.

Figure 27 is used to compare gains with losses in relation to the FOC control. The Flux\_opti\_2 control performs better on motors with lower power ratings (MAS4, MAS12, and MAS17). Whereas the Flux\_opti\_1 control stands out on more powerful motors (MAS6, MAS7, MAS18, MAS19, and MAS20). As for the Flux\_opti\_3 control, it is more constant regardless of motor power. We can conclude that, whatever the control chosen, the losses suppressed are quite significant compared with the FOC control, but depending on motor power, one of the three flux-optimized controls will perform better.



**Figure 27.** Comparison of regained losses.

Table 12 shows the yields of the best and worst controllers on each of the MAS. The raw efficiencies depend on the values of the components (rotor and stator resistances and inductances). By choosing the most suitable control for the asynchronous motor, the efficiency of each motor can be increased by 1.1% to 2.8%. The performance of the controls applied depends little on the motor configuration, and gains can be observed on all ten motors presented.

**Table 12.** Comparison of motor efficiencies.

Motor Name	Efficiency of the Least Efficient Control (FOC)	Efficiency of the Most Efficient Control	Efficiency Difference
MAS4	93.6%	96.2% (Opti n°2)	+2.6%
MAS5	94.8%	96.5% (Opti n°2)	+1.7%
MAS6	94.8%	96.1% (Opti n°1)	+1.3%
MAS7	95.9%	97.0% (Opti n°1)	+1.1%
MAS12	94.2%	97.0% (Opti n°2)	+2.8%
MAS13	94.8%	96.2% (Opti n°2)	+1.4%
MAS17	93.5%	95.7% (Opti n°2)	+2.2%
MAS18	94.2%	96.1% (Opti n°1)	+1.9%
MAS19	95.0%	96.7% (Opti n°1)	+1.7%
MAS20	95.9%	97.2% (Opti n°1)	+1.3%

## 6. Conclusions

In conclusion, the various controls applied to the two motors have performed well as they have allowed for a significant reduction in losses. The EMR/MSC representation has been successful in facilitating the understanding of the different controls. This paper shows that the Energy Macroscopic Representation (EMR) formalism, introduced a decade ago, is very practical for making the comparisons we have made in this paper. EMR offers a unified structure for the graphical presentation of system models and control laws. To switch from one control law to another, it is sufficient to change an instance of one or more blocks. The overall structure of the diagram remains the same.

The results obtained, simulated under conditions resembling those of a typical driving cycle, suggest that the controls are applicable in the automotive industry.

The more complex motors presented in the article justified the implementation of controls aimed at reducing energy consumption. In these motors, two currents  $i_d$  and  $i_q$  flow. Historically, the most well-known controls chose to use only one of these currents ( $i_q$ ) to produce torque. The  $i_d$  current was thus constant or zero, either used for flux regulation or not used at all. The advantage was that the control of these motors was close to a Direct Torque Control (DTC). However, the loss in torque production and the losses incurred by the flow of a constant current were significant drawbacks.

The aim of this work is to demonstrate that controls taking into account these losses exist for all motors and allow for energy savings while maintaining good performance. The

methodology was to present the known motor model along with its loss model and then represent them with the EMR. Subsequently, different controls seeking to minimize total losses were simulated.

For the PMSM, the LM/MTPA control was the most effective in considering copper and iron losses. Its implementation over ten motors demonstrated its effectiveness with an average of 25% of losses eliminated and an average efficiency increase of 3.2%. However, it should be noted that the benefits of this control depend heavily on the motor parameters on which the control is implemented. Hence, the eliminated losses were expressed as a ratio between the main torque and the reluctance torque to predict the performance of any IPMSM control.

In summary, the experiment highlighted controls reducing losses in two different motors. A uniform representation was used throughout the work with EMR and MSC to simplify the understanding of energy exchanges. The results we have reviewed in this study are interesting in practice. They have immediate applications. Indeed, the control laws of electric motors are already implemented on computers today. To implement more efficient laws, it is enough to change the software without changing the hardware. There is therefore no significant economic impact of updating the control laws on an existing fleet of electric machines. Future prospects for the project would involve conducting similar work on the Synchronous Reluctance Motor (SRM), integrating motor loss representation into the EMR, and continuing work above the nominal speed of the motor (constant power region).

We believe that a similar study on Brushless DC (BLDC) motors is worth conducting. These motors are becoming important in many aspects of the industry because they are less expensive than synchronous motors or induction motors.

More precisely, this work does not only apply to electric motor controls but also to all areas that use variable-speed motors. For a more global study of the electric vehicle, a broader study could be conducted to include losses related to batteries or supercapacitors.

Finally, it should be noted that similar gains could be gained in any industrial use of electric drive (marine propulsion, dump truck, machine tools, energy conversion, etc.).

**Author Contributions:** Conceptualization, J.-M.B., R.L. and E.D.; methodology, J.-M.B., R.L. and E.D.; software, R.L.; validation, J.-M.B., R.L. and E.D.; formal analysis, R.L.; investigation, J.-M.B., R.L. and E.D.; resources, J.-M.B. and E.D.; data curation, R.L.; writing—original draft preparation, R.L.; writing—review and editing, J.-M.B. and E.D.; visualization, J.-M.B. and R.L.; supervision, E.D.; project administration, J.-M.B. and E.D. All authors have read and agreed to the published version of the manuscript.

**Funding:** This research received no external funding.

**Data Availability Statement:** The original contributions presented in the study are included in the article, further inquiries can be directed to the corresponding author.

**Conflicts of Interest:** The authors declare no conflict of interest.

## References

1. Bouscayrol, A.; Hautier, J.P.; Lemaire-Semail, B. Graphic Formalisms for the Control of Multi-Physical Energetic Systems: COG and EMR. In *Systemic Design Methodologies for Electrical Energy Systems: Analysis, Synthesis and Management*; Roboam, X., Ed.; John Wiley & Sons, Ltd.: Hoboken, NJ, USA, 2013; Chapter 3, pp. 89–124.
2. Bouscayrol, A.; Delarue, P.; Guillaud, X. Power strategies for maximum control structure of a wind energy conversion system with a synchronous machine. *Renew. Energy* **2005**, *30*, 2273–2288. [[CrossRef](#)]
3. Fadili, S.; German, R.; Bouscayrol, A. HiL Testing of a High C-Rate Battery For the Nissan Leaf. In Proceedings of the 2022 IEEE Vehicle Power and Propulsion Conference (VPPC), Merced, CA, USA, 1–4 November 2022; pp. 1–6. [[CrossRef](#)]
4. Chi, T.P.N.; Nguyen, B.H.; Trovao, J.P.F.; Ta, M.C. Effect of Battery/Supercapacitor Hybrid Storage System on Battery Voltage in Electric Vehicles. In Proceedings of the 2022 IEEE Vehicle Power and Propulsion Conference (VPPC), Merced, CA, USA, 1–4 November 2022; pp. 1–6. [[CrossRef](#)]
5. Berriel, R.O.; Bouscayrol, A.; Delarue, P.; Brocart, C. Mechanical Braking Strategy Impact on Energy Consumption of a Subway. In Proceedings of the 2020 IEEE Vehicle Power and Propulsion Conference (VPPC), Merced, CA, USA, 1–4 November 2020; pp. 1–5. [[CrossRef](#)]

6. Badji, A.; Djoudi, H.; Benyahia, N.; Denoun, H.; Zaouia, M.; Benamrouche, N. Energetic macroscopic representation (EMR) based on internal model control (IMC) for fuel cell and supercapacitor hybrid electric vehicles. In Proceedings of the 2015 3rd International Conference on Control, Engineering & Information Technology (CEIT), Tlemcen, Algeria, 25–27 May 2015; pp. 1–6. [CrossRef]
7. Koita, A.; Payman, A.; Dakyo, B.; Hissel, D. Control of a Wind Energy Conversion System using the Energetic Macroscopic Representation. In Proceedings of the 2018 7th International Conference on Renewable Energy Research and Applications (ICRERA), Paris, France, 14–17 October 2018; pp. 1460–1465. [CrossRef]
8. Mock, P. The WLTP: How a new test procedure for cars will affect fuel consumption values in the EU. *Int. Counc. Clean Transp.* **2014**, *9*, 3547.
9. Tutuianu, M.; Bonnel, P.; Ciuffo, B.; Haniu, T.; Ichikawa, N.; Marotta, A.; Pavlovic, J.; Steven, H. Development of the World-wide harmonized Light duty Test Cycle (WLTC) and a possible pathway for its introduction in the European legislation. *Transp. Res. Part Transp. Environ.* **2015**, *40*, 61–75. [CrossRef]
10. Zhu, Z.; Liang, D.; Liu, K. Online Parameter Estimation for Permanent Magnet Synchronous Machines: An Overview. *IEEE Access* **2021**, *9*, 59059–59084. [CrossRef]
11. Zhu, Z.Q.; Howe, D. Electrical Machines and Drives for Electric, Hybrid, and Fuel Cell Vehicles. *Proc. IEEE* **2007**, *95*, 746–765. [CrossRef]
12. Oztekin, M.; Kiselychnyk, O.; Wang, J. Energy Efficient and Transients Optimal IPMSM Drive for Electric Vehicles. In Proceedings of the International Symposium on Power Electronics, Electrical Drives, Automation and Motion (SPEEDAM), Sorrento, Italy, 22–24 June 2022; pp. 832–837. [CrossRef]
13. Windisch, T.; Hofmann, W. Loss minimization of an IPMSM drive using pre-calculated optimized current references. In Proceedings of the 37th Annual Conference of the IEEE Industrial Electronics Society (IECON), Melbourne, Australia, 7–10 November 2011; pp. 4704–4709, ISSN 1553-572X. [CrossRef]
14. Nam, K.H. *AC Motor Control and Electrical Vehicle Applications*; CRC Press: Boca Raton, FL, USA, 2020.
15. Simulink-MathWorks France. *AC6-100 kW Interior Permanent Magnet Synchronous Motor Drive—MATLAB*. 2011. Available online: <https://fr.mathworks.com/help/sps/ug/ac6-100-kw-interior-permanent-magnet-synchronous-motor-drive.html> (accessed on 20 June 2023).
16. Song, Q.; Zhao, S.; Li, Y.; Ahmad, M. Voltage Vector Directional Control for IPMSM Based on MTPA Strategy. *IEEE Access* **2020**, *8*, 27998–28008. [CrossRef]
17. Bariša, T.; Sumina, D.; Kutija, M. Comparison of maximum torque per ampere and loss minimization control for the interior permanent magnet synchronous generator. In Proceedings of the International Conference on Electrical Drives and Power Electronics (EDPE), Tatranska Lomnica, Slovakia, 21–23 September 2015; pp. 497–502, ISSN 1339-3944. [CrossRef]
18. Sieklucki, G.; Kara, D. Design and Modelling of Energy Conversion with the Two-Region Torque Control of a PMSM in an EV Powertrain. *Energies* **2022**, *15*, 4887. [CrossRef]
19. Wei, H.; Yu, J.; Zhang, Y.; Ai, Q. High-speed control strategy for permanent magnet synchronous machines in electric vehicles drives: Analysis of dynamic torque response and instantaneous current compensation. *Energy Rep.* **2020**, *6*, 2324–2335. [CrossRef]
20. Trancho, E.; Ibarra, E.; Arias, A.; Salazar, C.; Lopez, I.; de Guereñu, A.D.; Peña, A. IPMSM torque control strategies based on LUTs and VCT feedback for robust control under machine parameter variations. In Proceedings of the 42nd Annual Conference of the IEEE Industrial Electronics Society (IECON), Florence, Italy, 24–27 October 2016; pp. 2833–2838. [CrossRef]
21. Zhao, Y.; Qiao, W.; Wu, L. An Adaptive Quasi-Sliding-Mode Rotor Position Observer-Based Sensorless Control for Interior Permanent Magnet Synchronous Machines. *IEEE Trans. Power Electron.* **2013**, *28*, 5618–5629. [CrossRef]
22. Halder, S.; Agarwal, P.; Srivastava, S. Comparative analysis of MTPA and ZDAC control in PMSM drive. In Proceedings of the Annual IEEE India Conference (INDICON), New Delhi, India, 17–20 December 2015; pp. 1–5, ISSN 2325-9418. [CrossRef]
23. Sanyasi Naidu, A.; Samanta, S. Analysis of IPMSM Motor by Using SPWM and SVPWM Based Vector Controller with MTPA Control Strategy. In Proceedings of the IEEE 10th Power India International Conference (PIICON), New Delhi, India, 25–27 November 2022; pp. 1–5, ISSN 2642-5289. [CrossRef]
24. Amornwongpeeti, S.; Kiselychnyk, O.; Wang, J.; Antaloae, C.; Soumelidis, M.; Shah, N. A combined MTPA and maximum efficiency control strategy for IPMSM motor drive systems. In Proceedings of the International Conference on Electrical Systems for Aircraft, Railway, Ship Propulsion and Road Vehicles & International Transportation Electrification Conference (ESARS-ITEC), Toulouse, France, 2–4 November 2016; pp. 1–6. [CrossRef]
25. Dang, K.L.; Nguyen, B.H.; Ta, M.C.; Trovão, J.P.F.; Vo-Duy, T. Sliding Mode Solution for Rotor Flux Control and Estimation of Induction Motors Using Energetic Macroscopic Representation. In Proceedings of the 11th International Conference on Control, Automation and Information Sciences (ICCAIS), Hanoi, Vietnam, 21–24 November 2022; pp. 535–540, ISSN 2475-7896. [CrossRef]
26. Hassan, A.; Bazzi, A. Adaptive Loss Minimization Technique of Induction Motor Drives Using Extended Kalman Filter. In *IEEE International Electric Machines and Drives Conference (IEMDC)*; IEEE: Piscataway, NJ, USA, 2021. [CrossRef]
27. V, K.; Singh, B. Optimum Flux Based Vector Control of Induction Motor Drive For Electric Vehicle. In *IEEE IAS Global Conference on Emerging Technologies (GlobConET)*; IEEE: Piscataway, NJ, USA, 2022. [CrossRef]

28. Roy, S.; Pandey, R. Efficiency Optimization of Vector Controlled Induction Motor Drive by Field Orientation Technique. In *Third International Conference on Advances in Electrical, Computing, Communication and Sustainable Technologies (ICAECT)*; IEEE: Piscataway, NJ, USA, 2023. [[CrossRef](#)]
29. Gülbahçe, M.O.; Karaaslan, M.E. Estimation of Induction Motor Equivalent Circuit Parameters from Manufacturer's Datasheet by Particle Swarm Optimization Algorithm for Variable Frequency Drives. *Electrica* **2021**, *22*, 16–26. [[CrossRef](#)]

**Disclaimer/Publisher's Note:** The statements, opinions and data contained in all publications are solely those of the individual author(s) and contributor(s) and not of MDPI and/or the editor(s). MDPI and/or the editor(s) disclaim responsibility for any injury to people or property resulting from any ideas, methods, instructions or products referred to in the content.